Numerical simulation techniques for the Efficient and accurate treatment of local Fluidic transport processes together with chemical reactions

O. Mierka, S. Turek

17 Numerical simulation techniques for the efficient and accurate treatment of local fluidic transport processes together with chemical reactions

Otto Mierka[1], Stefan Turek[2]

Abstract This work describes a numerical framework developed for the efficient and accurate simulation of microfluidic applications related to two leading experiments of the DFG SPP 1740 research initiative, namely the 'Superfocus Micromixer' and the 'Taylor bubble flow'. Both of these basic experiments are considered in a reactive framework using the SPP 1740 specific chemical reaction systems. A description of the utilized numerical components related to special meshing techniques, discretization methods and decoupling solver strategies is provided and its particular implementation is performed in the open-source CFD package FeatFlow [19]. A demonstration of the developed simulation tool is based on already defined validation cases and on suitable examples being responsible for the determination of the related convergence properties (in the range of targeted process parameter values) of the developed numerical framework. The subsequent studies give an insight into a parameter estimation method with the aim of determination of unknown reaction-kinetic parameter values by the help of experimentally measured data.

17.1 Introduction

Micromixers and microreactors provide a novel technology from which their suitable application even in industrial processes is expected. The mechanisms related to the flow dynamics are in general considered to be more deterministic than of those associated to their larger counterparts. This advantageous property is even more dominant in the field of numerical simulations, which therefore might possess an important role in the stage of design of the underlying equipment in order to achieve their theoretically best performance. Since numerical simulations are suitable tools to describe the flow dynamics and/or reaction kinetics in the underlying equipment for the accurately prescribed (physical, geometric or process) parameters, they also offer the advantage of determination of parameters -which due to

---

[1] O. Mierka

  TU Dortmund, Chair of Applied Mathematics and Numerics (LS3), Vogelpothsweg 87, 44227, Dortmund, e-mail: otto.mierka@math.tu-dortmund.de

[2] S. Turek

  TU Dortmund, Chair of Applied Mathematics and Numerics (LS3), Vogelpothsweg 87, 44227, Dortmund, e-mail: stefan.turek@math.tu-dortmund.de

different sorts of reasons cannot be determined with other techniques. Such an interplay between experimentally obtained measurement results and numerical simulations is the main idea described in the present work. However, it also has to be emphasized that the particular numerical techniques employed by the individual simulation software are extremely influential on the range of parameters in which the given simulation software can be applied for reliable predictions. Even in cases of just simple single-phase flow problems accompanied by mixing of species and chemical reactions there are high requirements put on the accuracy and efficiency of the given simulation tool, since the resolution of the steep concentration gradients is unavoidably inevitable for obtaining the mesh independent solution of the underlying problems. Suppressing the numerical diffusion and exploiting the highest non-oscillatory resolution of the results by the number of available grid points is the prerequisite of the employed efficient and robust solvers. In case of simulation problems extended by the presence of multiple phases with dynamically moving interfaces are even larger restrictions on the employed solution software introduced.

In this work we present a suitable numerical framework which is fulfilling the challenges requested by the targeted applications, which are the two basic leading experiments (Superfocus Micromixer and the round capillary Taylor Bubble) of the SPP 1740 research initiative, both applied in the framework of SPP 1740-specific reaction systems. In Chapter 17.2 we describe the mathematical model with special emphasis on the series of employed numerical components in the framework of the used Projection Method. In the subsequent Chapters 17.3 and 17.4 we provide numerical results in terms of 1) validation cases, 2) model problems estimating convergence of the developed numerical framework and 3) reverse engineering applications with the aim of estimation of kinetic parameters with respect to experimentally measured reference results. Finally, the presented work is closed by conclusions in Chapter 17.5 which provides the summary of the numerical simulations and the possibilities of the presented reverse engineering method.

17.2 Mathematical Model

The developed numerical simulation method is based on the open-source FEM software package FeatFlow [19] which provides the backbone of the flow solver supported by geometrical multigrid methods, domain decomposition based MPI parallelization and higher order FEM discretization of the Navier-Stokes equations. These are essentially the main features, which define the accuracy and efficiency of the basic FeatFlow flow solver, which has already proven to provide benchmark solutions for numerous numerical benchmark problems [2, 7]. The main numerical feature of the basic single phase FeatFlow flow solver is related to the Discrete Projection (DP) method which provides a solution strategy for the nonlinear algebraic system of equations of the arising fully (spatially and temporally) discretized system of Navier-Stokes equations.

Since the targeted numerical framework involves additional concentration transport problems of species undergoing chemical reactions, which are partially

related to gas/liquid flows, the basic flow solver has been extended with the corresponding multiphase and reaction modules. The general solution strategy is related to a direct numerical simulation (DNS) of the corresponding multiphase flow problem in a framework of an interface tracking approach, which requires an instationary direct resolution of the g/l interface by the computational mesh. The arising set of governing equations written in the generalized (single- or multiphase) framework is as follows:

$$\rho(\mathbf{x})\left[\frac{\partial \mathbf{u}}{\partial t} + \mathbf{u} \cdot \nabla \mathbf{u}\right] - \nabla \cdot (\mu(\mathbf{x})[\nabla \mathbf{u} + \nabla \mathbf{u}^T]) + \nabla p = \rho(\mathbf{x})\mathbf{a}_g + \mathbf{f}_\Gamma(\mathbf{x}, t) \qquad (1)$$

$$\nabla \cdot \boldsymbol{u} = 0 \qquad (2)$$

$$\frac{\partial c_i}{\partial t} + \nabla \cdot (\mathbf{u}c_i) - D_{i,l}\Delta c_i = s_i\left(c_{j=1,2,\dots,N}\right) \quad \text{for} \quad i = 1, 2, \dots, N_p \qquad (3)$$

where $\rho(\mathbf{x})$ and $\mu(\mathbf{x})$ represent the density and viscosity of the given phase which, however, depend on (in case of application for a multiphase problem) the particular interface location Γ separating the liquid and the gas phase from each other. Furthermore, at the arising dynamically evolving interface the surface tension force $\mathbf{f}_\Gamma(\mathbf{x}, t)$ is activated, which is defined as:

$$\mathbf{f}_\Gamma = \sigma_{l/g}\kappa\,\mathbf{n}_\Gamma \qquad (4)$$

where $\sigma_{l/g}$, κ and $\mathbf{n}_\Gamma$ stand for particular (material dependent) interfacial tension coefficient, curvature and outward normal to the interface Γ, respectively. The last parameters in the above equations are $\mathbf{a}_g$ - gravitational acceleration, $D_{i,l}$ – diffusion coefficient of the ith species in the liquid phase, and s_i represents the source/sink terms of the ith species due to the occurring chemical reactions. The system of the resulting nonlinear equations is therefore defined for the quantities $\mathbf{u}$, p and c_i, corresponding to velocity, pressure and concentration of the individual species from all present N_P species taking part in N_R chemical reactions defined by the underlying chemical reaction mechanisms. Now, depending on if the particular numerical problem involves the presence of multiple phases or only a single phase, determines the activation of the next transport equation controlling the deformation of the computational mesh with respect to the dynamic interface, Γ. Therefore, in case of gas-liquid simulations with resolved interfaces according to the used Interface Tracking (IT) approach the above defined system of equations is to be appended by the Mesh Deformation (MD) equation for the displacement vector $\mathbf{d}$, as follows:

$$\nabla \cdot (\nabla \mathbf{d} + (\nabla \mathbf{d})^T) = 0 \qquad (5)$$

The equation above is solved with respect to the updated deformation vector on the interface and for the side condition allowing a free slip of the mesh nodes on the already updated and constructed interface Γ. It has to be noted that due to the adopted IT approach the underlying computational mesh is of constant topology during the whole simulation, only the coordinates of the individual element vertices are being modified giving therefore rise to a mesh velocity $\boldsymbol{\omega}$. More details to the developed IT method is provided in Chapter 17.2.1.

Since all the listed equations defining the addressed problem are mutually coupled with each other in a strong nonlinear fashion, their solution requires a robust mechanism, unless their simultaneous monolithic solution is to be performed. However, due to the targeted full 3D applications and thus the related high number of

degrees of freedom, only a decoupling solution mechanism in a framework of the already mentioned DP method is feasible. According to the applied DP method, the solution of the system is decomposed into individual solution steps as explained below. Due to the fact, that the particular target applications are characterized by strictly laminar flow conditions and are expected to develop towards steady flows, the main decomposition of the system consists of decoupling the flow solution from the transport and reaction of the chemical species. According to such an (at the first look) *invasive* decoupling mechanism it is assumed that 1) the characteristic time-scale of hydrodynamics (i.e. reaching steady state flow conditions) is much smaller than the characteristic time-scale of the transport of species and their respective chemical reaction and that 2) the chemical species are present in the respective phases only in such low concentrations that their back-coupling on the flow can be neglected (such as buoyancy or Marangoni effects). Therefore, the solution algorithm is directly decomposed into 2 simulation sub-steps, which in particular means the solution of the Navier-Stokes system in the first step and with the obtained velocity solution to solve the corresponding mutually coupled species transport problem in the next step. In this respect, we provide more details for the underlying numerical methods used for the particular IT approach in Chapter 17.2.1 and for the solution of the scalar transport problems in an Operator Splitting (OS) framework in Chapter 17.2.2. Therefore, it is inevitable to introduce our generalized DP method of the fully discretized Navier-Stokes system already now, so to present the overall computational scheme before describing its special features in details. The fully discretized Navier-Stokes equations can be written in the following representation:

$$\begin{bmatrix} A & \Delta t B \\ B^T & 0 \end{bmatrix} \begin{bmatrix} \mathbf{u} \\ p \end{bmatrix} = \begin{bmatrix} \mathbf{g}_u \\ 0 \end{bmatrix} \qquad (6)$$

where A is the complete transport operator $A = M + \theta \Delta t (K + D)$, consisting of the contribution of mass, convection and diffusion operators. B and B^T are the discrete gradient and divergence operators, Δt is the time step between t^n and t^{n+1}, and $\mathbf{g}_u$ represents the right hand side encompassing the explicit contributions of the particular time stepping method and the explicit force terms. Now, if A is nonsingular the velocity can be formally expressed as $\mathbf{u} = A^{-1}(\mathbf{g}_u - \Delta t \, B \, p)$ and plugged into the discrete continuity equation $B^T \mathbf{u} = 0$, which gives the Schur complement equation for the pressure:

$$(B^T A^{-1} B) p = \frac{1}{\Delta t} B^T A^{-1} \mathbf{g}_u \qquad (7)$$

However, due to the fact that the $B^T A^{-1} B$ operator is impossible to build for realistic 3D problems (as it is a full, not a sparse matrix) the solution is realized by a preconditioned Richardson iteration where $S := B^T A^{-1} B$ (the so-called Schur complement) operator is approximated by a suitable counterpart. Now, assuming a framework of flows characterized by moderate Re numbers and the use of small time step sizes [17], the Schur complement can be suitably approximated by $S \cong P = B^T M_L^{-1} B$, ($M_L$ being the lumped mass matrix) which allows us to define the iteration step $l \rightarrow l + 1$ for computing the pressure at the new time level t^{n+1}

$$p^{l+1} = p^l + [B^T M_L^{-1} B]^{-1} \frac{1}{\Delta t} B^T A^{-1} [\mathbf{g}_u - \Delta t \, B \, p^l], \qquad (8)$$

Finally, the overall solution strategy can be described by the following steps:

1) Solve the nonlinear momentum equations for $\widetilde{\mathbf{u}}$ with the pressure from previous time level p^n

$$\widetilde{\mathbf{u}} = A(\widetilde{\mathbf{u}}, \Gamma^n, \boldsymbol{\omega}^n)^{-1}(\mathbf{g}_u(\mathbf{u}^n, \Gamma^n, \boldsymbol{\omega}^n) - \Delta t\, B\, p^n)$$

2) Solve the Pressure-Poisson problem for the pressure update q

$$P(p^{n+1} - p^n) := Pq = \frac{1}{\Delta t} B^T \widetilde{\mathbf{u}}$$

3) Correct the pressure and the velocity

$$p^{n+1} = p^n + q, \quad \mathbf{u}^{n+1} = \widetilde{\mathbf{u}} - \Delta t M_L^{-1} B q$$

4) Update the interface position (only in the interface normal direction)

$$\Gamma^{n+1} = \Gamma^n + (\mathbf{n}_\Gamma \cdot \mathbf{u}_\Gamma^{n+1})\mathbf{n}_\Gamma \, \Delta t$$

5) Solve the mesh deformation equation for the displacement $\mathbf{d}^{n+1}$

$$A_{\mathbf{d}}\, \mathbf{d}^{n+1} = 0$$

for the boundary conditions given by Γ^{n+1}, where $A_{\mathbf{d}}$ represents the discrete deformation operator being reconstructed at every time step.

17.2.1 Realization of the Interface Tracking (IT) approach

According to the general framework of the IT method the computational mesh is perfectly aligned with the free interface Γ which consequently means that the mesh has to be deformed at every single timestep and that not only at the interface but also in the volume of the present phases. This deformation may be realized on an algebraic basis, however a more robust realization is performed by means of the PDE based MD equation [5] which is to be solved to "steady state" at every timestep for the updated coordinates of the vertices at the interface. Due to the stability of the numerical scheme, the Q_2/P_1 FEM discretization of the Navier-Stokes system is extended with an additional Q_1 FEM PDE for the displacement MD equation. The accompanying effect of the used IT approach is related to the mesh movement treated by the ALE (Arbitrary Lagrangian-Eulerian) method, which gives rise to the mesh velocity $\boldsymbol{\omega}(\mathbf{x}, t)$. The applied ALE method leads to the transformation of the underlying Navier-Stokes equations, which depending on the applied temporal discretization results in the problem of evaluating the old velocity distribution on the new mesh. Therefore, the currently implemented realization is performed only by use of an implicit Euler scheme, which completely overcomes these interpolation difficulties, however, for the price of using smaller timestep sizes, which on the other hand, due to the presence of the relatively large surface tension forces, is constrained anyways. The next special feature of the used IT approach is the resulting semi-implicit treatment of the surface tension force by taking advantage of the Laplace-Beltrami transformation following the work of Hysing [6]. The surface tension force in the context of FEM discretization for the IT approach is introduced as a surface integral into the momentum equation in the following form:

$$\mathbf{f}_{st} = \int_\Gamma \sigma \kappa \mathbf{n}_\Gamma \cdot \mathbf{v} \, d\Gamma \qquad (9)$$

which by taking advantage of the surface tangential derivatives $\underline{\nabla}$ and $\underline{\Delta}$ can be formulated as:

$$\mathbf{f}_{st} = \int_{\Gamma} \sigma\left(\underline{\Delta}\,\mathbf{x}|_{\Gamma}\right) \cdot \mathbf{v}\, d\Gamma \qquad (10)$$

Since the new interface position $(\mathbf{x}|_{\Gamma})^{n+1}$ can be expressed as the function of the old interface position and the new velocity at the interface:

$$(\mathbf{x}|_{\Gamma})^{n+1} = (\mathbf{x}|_{\Gamma})^{n} + \mathbf{u}_{\Gamma}^{n+1}\Delta t \qquad (11)$$

by substituting it into (10) it allows us to represent the surface tension term in a semi-implicit manner by building its contribution into the transport operator A and into the right hand side of the Navier-Stokes equation.

Last, but not least, it is important to mention that the Q_2/P_1 FEM discretization for the Navier-Stokes system is performed by the use of isoparametric interpolation functions, which offer the advantage of exploiting the higher order discretization also for the geometric representation of the computational domain. Accordingly, the corresponding face- or edge-vertices located on the interface are not defined implicitly as simple coordinate averages of the corresponding corner points but are assigned to uniquely computed coordinates defining the curved interface. This is especially beneficial for the related element faces located on the interface, because it allows a higher order approximation of the interface. Moreover, it provides the necessary framework for the surface integration of the surface tension force term by means of the above-described Laplace-Beltrami transformation.

17.2.2 Realization of scalar transport problems in Operator Splitting (OS) framework

As described in Chapter 17.2, the scalar transport problem is solved subsequently, after obtaining the corresponding steady state flow distribution for the considered problem. Under the condition of fulfilling the related assumptions this approach offers the possibility of performing the scalar transport problem on an essentially differently constructed computational mesh than it was used for the flow simulation. This advantage is related to the fact that the transport of species is governed by a strongly convection dominated mechanism (compared to diffusion fluxes) according to which steep gradients of the species concentrations are expected to be resolved what might be possible only by the use of specially constructed high resolution computational meshes. For this reason, it is absolutely inevitable to enrich the arising discretization schemes with additional mechanisms 1) providing the necessary resolution there where needed and 2) to protect the discretization scheme from numerical diffusion as much as possible, so to gain maximum profit from the provided mesh resolution. The first component is provided in the current work by the Algebraic Mesh Deformation (AMD) method, which is essentially the extension of the classical *umbrella mesh smoothening* method [5] which is commonly used for mesh regularization purposes, however its application with a variable weight function enables its use for mesh adaptation purposes. Thus, the application of this AMD method requires a construction of a weight (or *monitor*) function, $w\left(\mathbf{x}, c_{i=1,\dots,N_p}\right)$, which might be related to different sort of measures, but it has to be designed in such a way that it has large values there where the mesh

nodes are required to be dragged to and small elsewhere. In this work, the construction is directly related to the distribution of maximum concentration gradient of all species, so to guarantee the maximum resolution possible (which is limited by the total number of elements) for all species. The second component being responsible for suppressing numerical diffusion but sustaining an oscillation-free high-resolution discretization is the Algebraic Flux Correction (AFC) method developed by Kuzmin and Turek [10]. This component transforms the originally linear spatial transport equation to a nonlinear one. However, it provides the local extremum diminishing property (maximum due to convection does not increase, minimum does not decrease) which controls and enforces the conservation of convective fluxes on the algebraic level. This last property is especially of high interest for the reason that the velocity field is interpolated onto the deformed computational mesh used by the scalar transport module from the computational mesh used by the flow solver. The interpolation of the velocity field is performed in the framework of an L_2 projection, which is supported by an octree based search engine to provide an efficient mapping between the two computational meshes.

An additionally used mesh deformation mechanism is related to the PDE based MD method already described in the previous chapter. In particular, it is used for the multiphase simulation problems where the computational meshes have to be inflated with additional boundary layers along the mesh layer surrounding the gas phase.

The discretization of the scalar transport equations is performed by Q_1 FEM discretization supplemented by the above mentioned AFC method. Due to the possibility of numerical simulations of problems where the corresponding time-scales of reaction might be orders of magnitude faster than the corresponding timescales of spatial transport (convection or diffusion) the arising transport equations of the individual species were decomposed from each other in an Operator Splitting framework. Accordingly, the spatial transport step is performed for all species independently from each other for the given time step size Δt, which is followed by the next step – decomposed to arbitrary number of sub-time-steps covering the same time step size Δt used for the spatial transportation – taking the chemical reaction into consideration. This transport of species (happening in the dimension of the species) is then performed independently in space – i.e. in each Q_1 nodal value of the computational mesh – by means of an ODE step for which we used the numerical realization described and implemented in the open-source library of Shampine and Lühring [13].

17.3   Numerical results of single-phase problems

17.3.1   T-mixer

The results of the simulation analysis provided in this chapter has been used for validation purposes with respect to the originally described studies of Bothe et al. [4] and has already been described in a detailed way in our paper [12]. Therefore, here we present only a brief summary of proofs demonstrating the capabilities of

the developed framework for the simulation of reacting single-phase flows. The underlying problem is related to a T-shape micromixer (for the geometrical representation the reader is referred to [4]) into which the two inlet streams are provided in a 1:1 volumetric ratio for a range of characteristic Reynolds numbers from which the most interesting case is the one with the upmost value $Re = \frac{\bar{U} d_h}{\nu} = 186$. As a result, the interaction of the two inflow streams transforms into an engulfment flow, which is characterized by complex flow structures thus drastically affecting the mixing of the reacting species. The inflow streams provide the reactants for the chemical reaction in an equimolar ratio so to enable a classical neutralization reaction of sodium-hydroxide (A) and hydrochloric acid (B), which is considered to be a nearly instantaneous chemical reaction:

$$A + B \xrightarrow{k} P \quad \text{with} \quad k \approx 10^{11} \text{ L}/(\text{mol} \cdot \text{s}) . \tag{12}$$
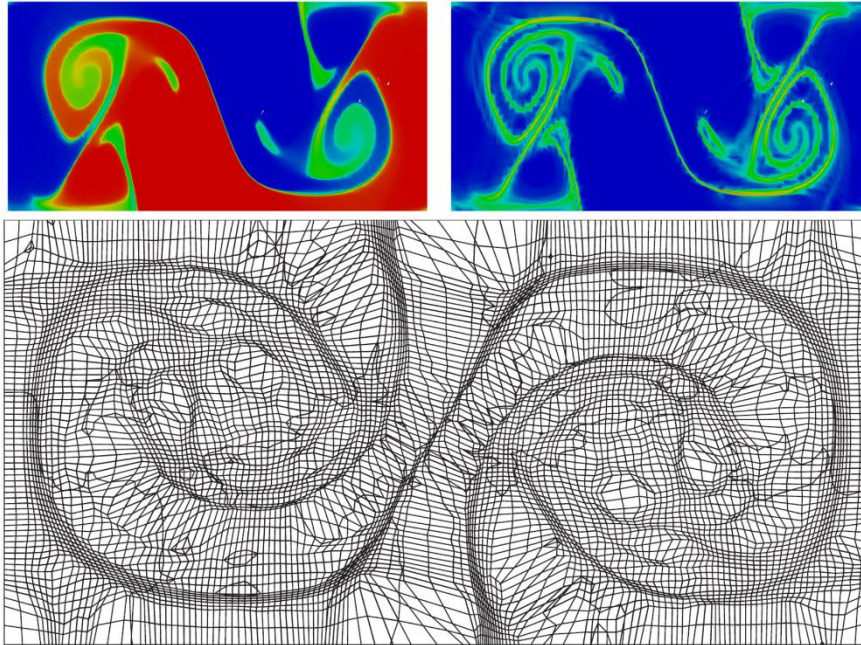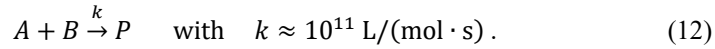
Figure 17.1: Computational results computed for the T-mixer. Visualization of the results are displayed at a cutplane normal to flow direction at the position $z = 250\ \mu m$. Top-left: representation of the quantity ϕ. Top-right: Distribution of the monitor function. Bottom: Distribution of the computational mesh

This property is exploited for the numerical simulations in a framework of a transformation (see Toor and Chiang [16]), which allows us to simulate the evolution of the distribution of only one scalar quantity, namely $\phi = c_A - c_B$. According to this transformation the reaction sink and source terms for the transported quantity ϕ cancel out each other and the corresponding reactant concentrations can be simply

recovered by $c_A = \max\{\phi, 0\}$ and $c_B = \max\{-\phi, 0\}$. Considering that the values of the diffusion coefficients of the relevant species are on the order of $D_{A,B} \approx 3 \cdot 10^{-9}$ m^2/s (and thus resulting in a Schmidt number of $Sc = \frac{\nu}{D_{A,B}} = 300$) the occurrence of steep concentration gradients is expected which imposes high resolution requirements on the simulation software. Since the occurrence of such regions is a priori not known, but obtained only after the simulation, the approach of simulations by means of pre-refined static meshes is not realizable, instead simulation approaches using adaptively moving meshes offer the possibilities to deliver most accurate and most effective (compute power per simulation accuracy) results. Therefore, the realization of the simulations here was decomposed into the following two steps:

1) Since the velocity field exhibits a much more regular and smooth distribution as ϕ, recovering the *steady* flow field was performed on a moderately fine static mesh of $\approx 2 \cdot 10^4$ structured mesh consisting of uniform hexahedral elements.

2) Simulation of the transport of the scalar quantity ϕ was performed on an initially equidistant mesh of $\approx 1 \cdot 10^7$ hexahedral elements, the distribution of which was then adaptively changing based on the evaluated monitor function distribution until reaching steady state of ϕ distribution and therefore also of the mesh movement. The convective term has been updated by means of an L_2 interpolation from the previously computed flow field onto the deformed computational mesh.

The mechanism and the performance of the computational framework is demonstrated by means of Figure 17.1Figure 17.1, which provides the distribution of the transported scalar quantity ϕ at the same axial (reference) position as it is published in the original study from Bothe et al. [4] using roughly the same number of elements. As it can be seen from the corresponding figure, the regions characterized by the presence of steep gradients are resolved with the necessary quality so to guarantee a high accuracy of the computational framework. The additional subfigures of Figure 17.1Figure 17.1 display the distribution of the computational mesh along the reference slice, such as the distribution of the monitor function, which has been related to the gradient of the scalar quantity ϕ. As it can be seen from the individual figures, the adaptation of the computational mesh with respect to the overall number of available elements is capturing the critical regions in a very accurate way. However, due to the relatively large overall differences of the results for the analyzed resolutions it cannot be estimated if a next resolution level would already provide a satisfactory quantitative match with the here computed highest resolution results. Nevertheless, the results presented here – considering the achieved resolution – provide the most accurate numerical approximations to the considered problem.

17.3.2 Validation of the numerical framework for SFM

Due to the geometrical realization of the Superfocus Micromixer the mixing efficiency of this engineering equipment is much higher than of the T-mixer described

in the previous subchapter. Since the inflow streams contact each other in an inter-digital manner, the chemical species from the individual inlet streams need to tackle a much shorter distance by molecular diffusion so to provide a high mixing efficiency of the mixing unit. Since the concentration gradients in the liquid mixture are expected to be very high the numerical simulation of such flows, especially in combination with chemical reactions is not only a challenging problem, but if once such a simulation tool is successfully designed, it offers the possibility of a reverse engineering framework being suitable for determination of missing parameters of the system. According to such a reverse engineering framework, by the help of performing simulations for parameter variations (in certain parameter ranges) with respect to experimentally measured data, parameters like diffusion coefficients or reaction constants might be determined. The prerequisite of such a computational engineering tool is to guarantee its spatial convergence for the corresponding parameter space. For this reason, we have adopted the geometry of a standard SFM displayed in Figure 17.2.
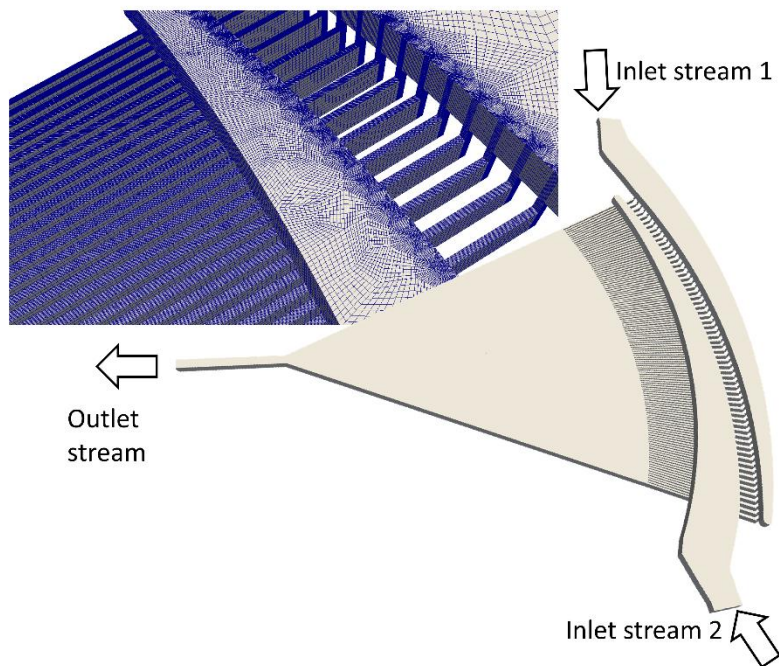
Figure 17.2: Geometrical representation of the computationally simulated SFM with a mesh detail showing the distribution of the generated hexahedral elements.

It has to be noted that the flow distributor located upstream of the SFM plays an extremely important role since it is responsible to provide the inflow streams into

the mixer as equally homogenized as possible. Subsequently, its geometrical representation had to be included into the numerical simulations, however only in those stages, which concern the hydrodynamics. Details of the half-automatically created hexahedral coarse mesh (Level 1) used for the flow simulations are displayed as subfigures in Figure 17.2. The fluid parameters for the simulations correspond to water and the concentration of the chemical species were considered at such low levels that their respective back-coupling effects on the flow could be neglected. For the underlying convergence study the same reaction mechanism has been assumed as described for the T-mixer above (see Chapter 17.3.1). Accordingly, the transformation of Toor and Chiang [16] was utilized resulting in a simulation of only one single scalar transport equation for ϕ. In order to guarantee larger range of parameter spaces for subsequent simulation problems the diffusion coefficient of the respective species (and thus also ϕ) has been chosen 10 times lower as in the previous T-mixer case, namely $D_{A,B} = 3.0 \cdot 10^{-10} \, \text{m}^2/\text{s}$. The considered total flowrates were $\dot{V} = [100, \, 250, \, 500] \, \text{cm}^3/\text{h}$ resulting in characteristic Reynolds numbers on the order of $\text{Re} = [50, \, 125, \, 250]$ with respect to the average outflow velocity and channel depth. Since the underlying Q_2/P_1 FEM flow simulations provided smooth velocity distributions of the computed flow fields, already the Level 2 spatial refinement solutions were considered as mesh independent solutions for all considered liquid throughput cases. The correspondingly obtained velocity solutions were utilized in the subsequent scalar transport simulations which have been interpolated onto the dynamically deformed computational meshes. The originally structured mesh spanning the tapering geometry of the SFM has been simulated on two successively refined mesh resolutions corresponding to number of hexahedral elements of $N_{El} = 1.25 \cdot 10^6$ and $N_{El} = 1.0 \cdot 10^7$. Only these two mesh resolution levels have been considered because a coarser representation of the computational mesh was a priori excluded from the analysis and an even finer representation was due to the resulting computational requirements unrealizable. Some typical deformations of the computational meshes are visible as additional subpicture of Figure 17.3. As it can be seen from the corresponding figures, an alignment of the final steady state mesh is observable along the inlet streams; moreover, also the circumferential adaptation of the mesh density is also clearly visible which gradually homogenizes in the flow-direction by the flattening of the scalar gradient used as monitor function. The corresponding steady state solutions have been used for postprocessing and for mutual comparisons with respect to the determined overall conversion of the chemical reaction χ_r, defined as a ratio of generated product amount to the initial amount of reactant (A or B, since they are present in an equimolar ratio). Accordingly, the concentrations of the individual reactants have been integrated and averaged with respect to the outflow area, as follows:

$$\bar{c}_{A(B)} = \frac{\int_A (\boldsymbol{v} \cdot \boldsymbol{n}) \, c_{A(B)} \, dA}{\int_A (\boldsymbol{v} \cdot \boldsymbol{n}) \, dA} \qquad (13)$$
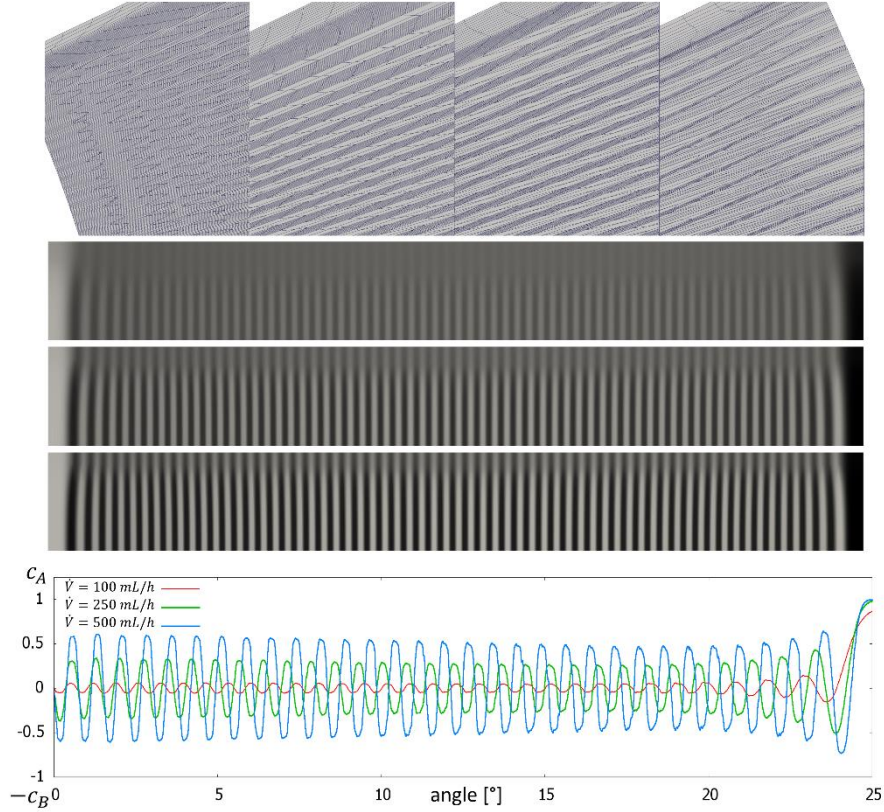
Figure 17.3: Top: details of the computational mesh used for the scalar transport problem at different positions. Middle: distribution of the scalar quantity ϕ at the 80% axial length position (circular slice) for 100, 250 and 500 cm^3/h. Bottom: Concentration distribution along the symmetry line at the outflow plane from the SFM.

where $\boldsymbol{v}$ and $\boldsymbol{n}$ stand for velocity and outflow normal, respectively. The integration surface A corresponds to the outflow surface, and since $c_{A_0} = c_{B_0}$ and the chemical reaction is equimolar $\bar{c}_A = \bar{c}_B$ at the outflow, as well. The corresponding simulation results are summarized in Figure 17.3: Top: details of the computational mesh used for the scalar transport problem at different positions. Middle: distribution of the scalar quantity ϕ at the 80% axial length position (circular slice) for 100, 250 and 500 cm^3/h. Bottom: Concentration distribution along the symmetry line at the outflow plane from the SFM., showing the fine level representation concentration profiles along the circumferential direction at the outflow for the considered flowrates as a 1) graphical representation along the symmetry line and as a 2) spatial distribution at a respective axial positions. According to the related figures, the effect of the increasing flowrate is clearly observable by means of the sharper segregation of the black/white signal representing the individual species. Besides of such

a qualitative representation of the results a more comprehensive evaluation is provided in Table 17.1, which shows the dependency of the determined conversion χ_r with respect to the applied mesh resolution. As it can be seen from the table, the differences between the mesh resolutions are increasing for the increasing flowrate, what is due to the occurrence of the increasing concentration gradients. Therefore, the differences between the resolution levels are increasing because the resolution of the arising concentration gradients is more restricted with the amount of available elements. However, the effective differences are in the range of only 10% for the largest flowrate (and only 2% for the smallest one) which due to the employed finite element framework gives a well-founded expectation for an already negligibly small deviation for an even higher resolution simulation. Finally, yet importantly, it also has to be noted that the diffusion coefficient has also been chosen to be a magnitude lower than diffusion coefficients of typical chemical species (used in our subsequent studies). The correspondingly estimated mesh resolutions were determined as reference for our subsequent studies, which have been supported by experimentally measured data.

Table 17.1: Mesh convergence of the chemical reaction conversion χ_r for the analyzed flowrates.

Mesh Resolution	χ_r [%]		
N_{El}	Re = 50	Re = 125	Re = 250
$1.25 \cdot 10^6$	97.3	88.5	75.4
$1.00 \cdot 10^7$	95.8	81.9	68.3

17.3.3 Reaction parameter estimation by the help of SFM

In this subchapter we provide an insight into the developed reverse engineering framework applied in the framework of the SFM which is one of the basic leading experiment units of the SPP 1740. The description of the numerical realization of the developed tool is essentially identical to the above described two applications (see Chapter 17.3.1 and 17.3.2) with the difference that instead of a numerical reconstruction of the experimentally measured behavior with known parameter settings here the determination of unknown parameters is performed. Realization of a suitable prototype exploiting the designed numerical components has already been reported by Mierka et al. [12] that tackled the problem of estimation of the diffusion coefficient of oxygen in the carrying liquid by means of utilizing optimization methods with respect to the experimentally measured spatially resolved concentration distributions at different locations of the mixer. Furthermore, a kinetic parameter of a Sulfite/Sulfate chemical reaction was also estimated by the utilization of similar optimization techniques supported by experimental data corresponding to a large range of operating conditions. The only drawback experienced in the mentioned studies is related to the computational efficiency, since the necessary computational resources might explode by covering a large range of parameter values in case of a

multi-parameter optimization framework. As a remedy a geometrical acceleration of the optimization procedure has been developed which exploits the similarity of the core-region of the SFM with the performance of the overall mixing unit. Accordingly, a predictor/corrector realization of the optimization procedure has been proposed which allows a quick estimation of the narrow parameter ranges (predictor) which in the next step can be further improved to an optimal combination of parameters by means of performing the corresponding simulations on the full geometrical representation (corrector).

The particular chemical reaction system used for the demonstration of reaction parameter estimation of a consecutive reaction system (for details see [15]) is an oxidation reaction of a btmgp copper(I) complex (A). The first reaction gives rise to formation of a thermally unstable intermediate bis(μ-oxo)dicopper species (C) which is then subsequently transforming to bis(μ-hydroxo)dicopper(II) species (D) being the final product of the reaction scheme (for details of the reaction system we refer to [15]):

$$2A + B \xrightarrow{k_1} C \xrightarrow{k_2} D \tag{14}$$

In the above equation (B) referring to the dissolved O_2 species in acetonitrile, k_1 and k_2 are the reaction constants specifying the speed of the reaction rates r_1 and r_2, which are defined as follows:

$$r_1 = k_1 c_A^1 c_B^0 = -\frac{dc_A}{2dt} = -\frac{dc_B}{dt} = \frac{dc_C}{dt} \tag{15}$$

$$r_2 = k_2 c_C^1 = -\frac{dc_C}{dt} = \frac{dc_D}{dt} \tag{16}$$

The experimentally measured reference data has been provided by our cooperation partners from RWTH Aachen and therefore for details of the utilized experimental techniques, the reader is referred to Schurr et al. [15]. The such provided reference data – evaluated in terms of averaged concentration values of the intermediate species (C) – corresponds to a large range of flowrates of the inlet streams $\dot{V}_{min} = 0.44$ mL/min up to $\dot{V}_{max} = 56.0$ mL/min and was measured for two inflow concentrations of the reactants $c_{Cu^I}^{in} = 2.0$ mM and $c_{Cu^I}^{in} = 5.0$ mM. The diffusivity values of the underlying Cu complexes in acetonitrile have been experimentally determined as $D_A = D_C = D_D = 1.40 \cdot 10^{-9}$ m²/s and the diffusivity of oxygen has been estimated by means of the proposed correlation of Schumpe and Lühring [14] as:

$$D_B = (2.6 \cdot 10^{-11})\mu_L^{-2/3} \cong 5.0 \cdot 10^{-9} \text{ m}^2/\text{s} \tag{16}$$

but because of the undetermined accuracy of the proposed correlation this parameter has been also included into the reverse engineering framework. Thus, the complete initial parameter space has been estimated as:

$$k_1 = \langle 3,30 \rangle \text{ } s^{-1}; \text{ } k_2 = \langle 0.6, 2.0 \rangle \text{ } s^{-1}; \text{ } D_B = \langle 4.0, 6.0 \rangle \cdot 10^{-9} \text{ m}^2/\text{s} \tag{17}$$

The two geometrical representations used for the reverse engineering framework correspond only to the tapering part of the SFM (without the inflow distributor and without the residence channel at the outflow), which considering their geometrically defined volume ratios correspond to a small ($N_{El} = 2.8 \cdot 10^4$) and to a large ($N_{El} =$

$1.0 \cdot 10^6$) computational mesh covering the core (2+2 streams) and the full (64+64 streams) geometrical representation of the SFM. The provided resolutions are in agreement with the estimated resolution requirements found in the previous sub-chapter Chapter 17.3.3, especially with respect to the roughly 10 times higher diffusion coefficients values of the considered species. Concerning the boundary conditions and the numerical realization the large geometrical variant has been treated in the same way as in the previous validation chapter. However, it is worth to mention, that for the smaller geometrical variant the simulations were restricted only to the scalar transport equations of the individual species, because the flow field has been sampled according to the analytical parabolic solution. Therefore, the velocity **v** for an arbitrary point $[x_0, y_0, z_0]$ in the smaller geometrical variant is prescribed as follows:

$$v = \frac{v_{\max}(h^2 - z_0^2)}{16(x_0^2 + y_0^2)}[x_0, -y_0, 0] \tag{18}$$

where $v_{\max}$ is a parameter used for calibrating the corresponding flowrate and h represents the half of the thickness of the SFM, i.e. $h = 250 \ \mu$m. The correspondingly designed flow field fulfills periodicity at the tapering sides and therefore it is also suitable for numerical simulation of the respective transport equations in the framework of periodic boundary conditions at the corresponding boundaries. The mesh deformation with the aim of mesh adaptation at the regions of steep gradients is then performed analogously as for the full geometrical variant.
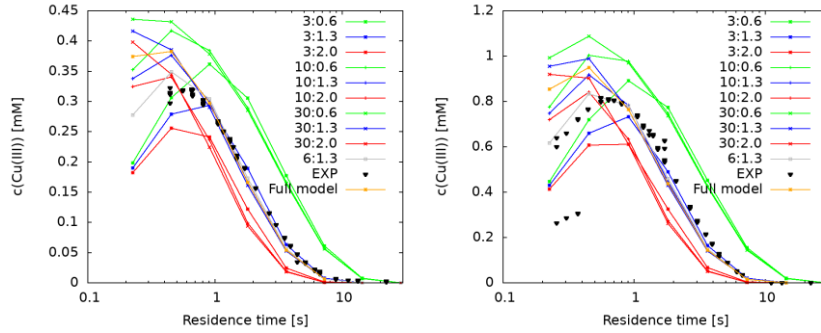
Figure 17.4: Comparison of computational results against the experimental references obtained for a sequence of simple and a full geometric representation for two inflow concentration values of the reactant species Cu(I). Left: $c_{Cu^I}^{in} = 2.0 \ mM$ and right $c_{Cu^I}^{in} = 5.0 \ mM$. Computational values of the full representation (with orange) correspond to the ratios of reaction constants $k_1 : k_2 = 10 : 1.3$ in s^{-1} and $D_B = 400 \cdot 10^{-7} \ cm^2/s$. The parameters of the individual curves are the corresponding ratios of kinetic constants, $k_1 : k_2$.

The results of the performed optimization process are displayed at Figure 17.4, which shows the variation of simulation results for the small geometrical representation with respect to the experimental reference data. Based on the initial simulations in the searched parameter space the optimal combination of reaction constants

has been estimated as $[k_1, k_2] = [6 \text{ s}^{-1}, 1.3 \text{ s}^{-1}]$. The value of the diffusion coefficient was found to be only slightly influential in the considered range of values and was determined to be best fitting the experimental reference data for $D_B = 4.0 \cdot 10^{-9} \text{ m}^2/\text{s}$. Concerning the prediction quality of this predictor step we have performed a corresponding simulation for the full geometric representation for the parameter values $[k_1, k_2, D_B] = [10 \text{ s}^{-1}, 1.3 \text{ s}^{-1}, 4.0 \cdot 10^{-9} \text{ m}^2/\text{s}]$. The average concentration values for the intermediate species (C) obtained by this way are matching the corresponding smaller geometrical representation results in an almost perfect way (see Figure 17.4). Considerable differences are observed only for the high flowrate cases what is attributed to the arising differences in the underlying flow fields occurring especially at the entrance regions. Aside of these extreme flowrate cases it can be concluded that the accuracy but especially the efficiency of the developed reverse engineering toolbox has been considerably improved compared to its basic realization described in Mierka et al. [12].

17.4   Numerical results of chemically reacting multi-phase problems

The presented numerical framework used for the multiphase flow simulations is essentially based on the method already presented in [12], which at the same time provided results for the benchmark problem of a single 3D rising bubble originally introduced by Adelsberger et al. [1]. The presented work has provided – up to the best knowledge of the authors – the so far most accurately determined (benchmark) evolution of quantities involving the bubble circularity, bubble rise velocity and characteristic bubble sizes. All these carefully chosen quantities are extremely sensitive with respect to the accuracy of the underlying numerical method, and therefore in light of the generated results the used numerical framework has proved its applicability and efficiency for a segment of multiphase flow problems, which neither undergo topological changes, nor experience strong deformations of the interface. Therefore, this numerical framework has been extended with an additional simulation module enabling the simulation of chemical reactions. Since the flows standing in the focus of our presented studies are characterized by a rather low Re numbers and rather low concentrations of chemical species taking part at chemical reactions, it allowed us to decompose the two transport problems of momentum and species concentration into two (from each other) decoupled computational modules. The first computational module is responsible for the determination of the steady state shape of the interface and the related flow field for an initially prescribed bubble volume enclosed by an initially defined regular interface separating the two present phases. The next computational module consists of a mesh construction method which is related only to the liquid phase since the gas phase is from the scalar transport simulations excluded (under the assumption of a very low effective mass transfer of the reactant from the gas to the liquid phase). The coarse mesh (in the context of geometrical multigrid) is extended with additional recursively refined boundary layers along the layer surrounding the bubble from the liquid side and is used for further successive refinements in the framework of the same PDE based

mesh deformation method as used in the previous hydrodynamics simulation step. The previously determined velocity distribution is then in the last step projected in an L_2 projection sense on the such obtained high-resolution computational (static) mesh, which is subsequently used for the numerical simulation of the species transport accompanied by chemical reactions. The highlighted computational method is demonstrated and used in the next two numerical subchapters with the aim to present its convergence properties (Chapter 17.4.1) and, moreover, to undergo a reverse engineering framework in order to estimate kinetic parameters of the underlying chemical reactions (Chapter 17.4.2).

17.4.1 Numerical simulation of a large Taylor-bubble

Before providing computational details for a chemically reacting Taylor bubble flow let us demonstrate the accuracy and suitability of the developed framework for Taylor bubble flows. An excellent example for this purpose has been reported from Marschall et al. [11] that provides all prerequisites of a numerical multiphase flow benchmark, since aside of the precise description of the problem with all necessary parameters it provides numerical predictions for several computational methods supported by an experimentally measured high-quality segmentation of the bubble surface [3]. The geometrical realization of the problem corresponds to a bubble of a prescribed volume V_b located in a straight and vertically aligned square-cross-sectional capillary. The free rise of the bubble is modified by providing a flowrate of the liquid phase represented by an average plug velocity of v_L resulting in a final transportation velocity of the bubble U_b. The liquid phase used in the experiments corresponds to an aqueous solution of glycerol (resulting in a ≈ 30 times larger viscosity than water), while the gas phase corresponds to air. The combination of material properties together with the related operation conditions can be characterized by means of the corresponding Capillary $Ca = \mu_l U_b / \sigma$ and the Reynolds $Re = \rho_l d_h U_b / \mu_l$ numbers, which for the here considered flow result in $Ca = 0.088$ and the $Re = 17.0$. The particular values of the above introduced parameters and physical properties are provided below:

$\rho_l = 1195.6 \, \text{kg/m}^3, \quad \mu_l = 28.54 \, m\text{Pa.s}$

$\rho_g = 1.3 \, \text{kg/m}^3, \quad\quad \mu_g = 2.0 \cdot 10^{-5} \text{Pa.s}, \quad \sigma = 66.69 \cdot 10^{-5} \, \text{N/m},$

$d_c = 1.98 \, mm, \quad\quad\quad V_b = 17.49 \, mm^3, \quad\quad L_c = 13.5 \, mm$

$U_b = 205.57 \pm 0.82 \, mm/s, \quad\quad\quad\quad\quad v_L = 138.2 \, \text{mm/s}.$

The numerical simulations were performed in a transient fashion starting from rest, so that an initial bubble volume V_b was prescribed which then due to the interaction of the individual forces started to move and deform its surface. Due to the adopted *Reference Frame Transformation* with respect to the center of mass of the bubble, it is possible to minimize the deformation of the bubble, which is this way relatively - to the computational domain - always at the same axial position. According to the corresponding translational transformation, the boundary conditions become nonstationary and therefore are updated at every timestep together with the acceleration related force term, which vanishes by reaching steady state. The simulations have been initially performed on the coarsest resolution Level 2, which after

reaching steady state (relative changes become smaller than the threshold defined for this purpose) have been interpolated to the higher resolution Level 3 and subsequently to the highest resolution Level 4. However, because the bubble volumes after interpolations have changed ($\approx 0.2\%$) all coarser level simulations (Level 2 and 3) have been restarted for the bubble volume determined from the finest Level 4 solution. This enabled us to organize the results into a suitable format for a mesh-convergence study with respect to a list of several sensitive quantities, such as the bubble length L_b and rising speed of the bubble U_b, and the related film thicknesses in the lateral Φ_l and diagonal direction Φ_d. The such extracted data is displayed in Table 17.2 which shows that already the coarse level resolution results are very close to the experimentally measured references and by the increased resolution the changes remain very small with respect to the higher resolution levels.

Table 17.2: Mesh convergence of the large Taylor bubble problem with respect to the experimental references [3]. L_b stands for length of the bubble, Φ_d and Φ_l stand for the diagonal and lateral film thickness between the bubble and wall of the capillary, U_b is the terminal bubble velocity and $\dot{\chi}_b$ stands for the rate of change of bubble volume.

	Sim L_2	Sim L_3	Sim L_4	Exp
L_b [mm]	7.185	7.204	7.214	7.200
Φ_d [μm]	431.6	434.4	435.4	433.1
Φ_l [μm]	46.8	49.7	49.7	50.5
U_b [mm/s]	19.17	19.78	20.07	20.56
$\dot{\chi}_b$ [%/s]	0.025	0.0003	<0.00001	-
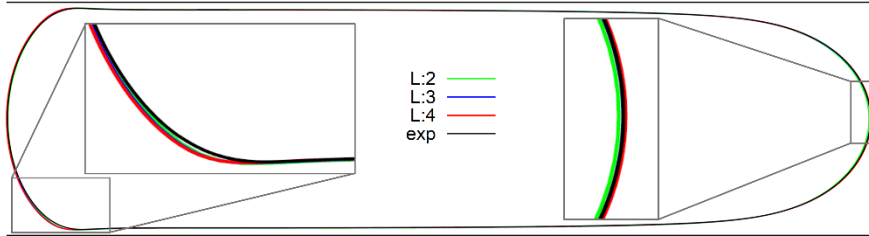
Figure 17.5: Mesh convergence of the bubble shape for the large Taylor bubble problem with close-ups at regions characterized by the largest deviation. Experimental reference is plotted with black line and the mesh resolution levels 2, 3 and 4 are colored by green, blue and red, respectively.

However, due to the still remaining differences in the corresponding bubble volumes ($< 0.01\%$) it is not possible to clearly identify a convergence order of the computational method. It also has to be noted that the simulations are performed in a transient fashion, which are unfortunately influenced by a marginal volume loss, which on the different resolution levels exhibits a different mass-loss-rate violating the assumption of reaching an asymptotical steady state. Nevertheless, the volume loss of the coarse level is on the order of 0.02% for the simulation time of $1s$ – what

is already nearly identical to a characteristic time interval needed to achieve a steady state solution of the corresponding problem – which is already a challengingly low mass loss rate compared to the capabilities of classical front capturing methods even on very fine mesh resolutions. Moreover, the decrease of the corresponding mass-loss-rate with respect to the higher resolution levels shows the expected high convergence order (see Table 17.2). Last but not least, the convergence of the computations are also well demonstrated by means of the bubble shapes for the individual resolution levels as displayed in Figure 17.5, which are practically overlapping with each other and are in a fairly good agreement with the experimentally provided measurement data.
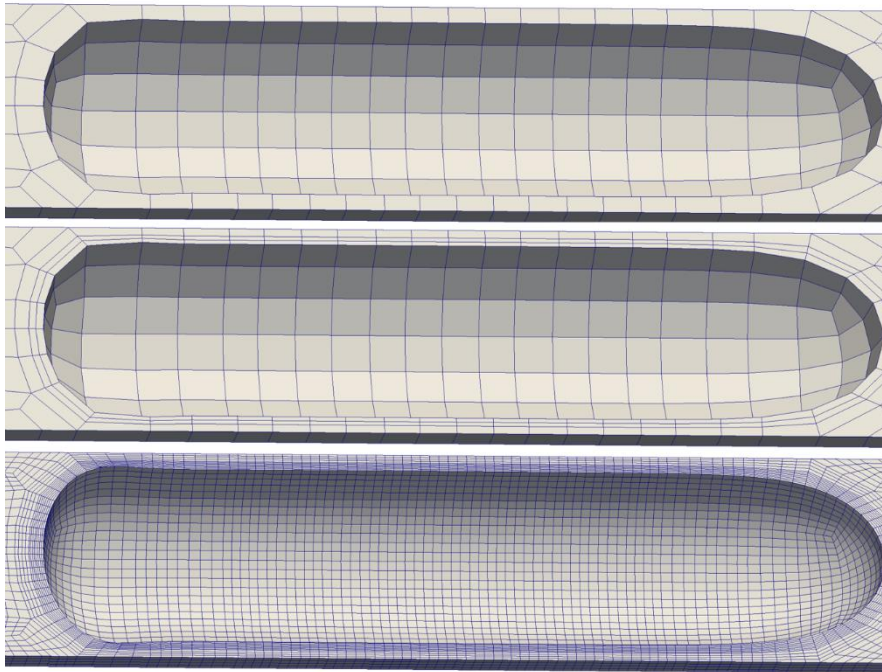
Figure 17.6: Visualization of the computational meshes constructed for the scalar transport problem. Top: original coarse mesh (without the bubble phase) used for the flow simulation. Middle: Boundary layer extension of the above mesh. Bottom: final computational mesh (visualized on Level 3) after adaptation to the bubble surface and deformation of the inner nodes.

Due to the above-considered square-cross-sectional capillary the liquid film squeezed between the bubble and the capillary wall has a varying thickness which has still a relatively large minimum thickness being only on the order of $\cong 2.5\%$ of the hydraulic diameter. However, in case of a subsequent simulation of transport of species the boundary layer around the bubble might have orders of magnitude smaller thickness the numerical resolution of which without using special meshing

techniques is nearly impossible and therefore can be approached only by the use of suitable sub-grid scale models [18]. This is the reason why the underlying setup has been used in combination of the SPP1740-specific copper based chemical reaction system [15] for a convergence study, however considering the targeted round capillaries of the SPP1740 the realization of the problem was changed to a circular capillary. Accordingly, the hydraulic diameter and length of the capillary, volume of the bubble and the respective material properties of the two phases were kept identical as in the previous flow validation example and only a different imposition of boundary conditions has been realized, namely, via periodic boundary conditions at the inflow and outflow of the capillary. This realization is utilized in order to mimic an infinite sequence of bubbles and liquid slugs, which will be the central mechanism in our subsequent reverse engineering analysis. Therefore, a pressure drop value of $\Delta p = 385$ Pa has been used in order to obtain a comparable transportation velocity $U_b = 206.9$ mm/s of the bubble in the capillary as for the above described validation example. According to the developed computational strategy the coarse mesh of the obtained steady state solution has been extended with additional recursively inflated boundary layers (Figure 17.6) and refined to the required mesh resolutions up to Level 6 with the use of the corresponding PDE based mesh deformation. For demonstration purposes, the Level 3 resolution of the correspondingly prepared computational mesh for the scalar transport problem is displayed in Figure 17.6.

The numerical simulations of the subsequent reacting flow problems were performed by using the already determined diffusion coefficients and reaction kinetics from Chapter 17.3.3 for the corresponding consecutive Cu complex chemical reactions. The initial boundary conditions of the chemical species were defined as $c_{A_0} = 0.001$ M/L and as zero for all other species and the boundary conditions were defined as $c_{B_\Gamma} = 0.008$ M/L on the bubble surface and as zero flux of all other species at all other outer walls of the computational domain. Finally, the previously mentioned periodicity (without concentration jump) at the inflow/outflow faces of the capillary was imposed. The numerical simulations were performed for a time window of 2 s, which for the considered highest mesh resolution (Level 6) took roughly a day on 4 nodes of a 16 core intel Xeon cluster on LiDo3. A visual comparison of the obtained results with the results of a one level coarser simulation (Level 5) is displayed in Figure 17.7, which provides the spatial distribution of the individual species at time $t = 2$s and provides close-ups of the critical regions with respect to the corresponding mesh resolution. As it is clearly seen from the provided graphical proofs, the qualitative agreement of the respective species concentrations is excellent between the two mesh resolutions and therefore the obtained results might be considered as spatially converged numerical solutions. The concentration boundary layer of oxygen (B) shown in the subpictures exhibits nearly identical representations on both mesh resolutions thus the corresponding resolution requirements are considered to be fulfilled and therefore were applied in this sense for the subsequent studies. Furthermore, it also has to be noted that the considered numerical problem is characterized by a rather high value of the Schmidt number $\mathrm{Sc} = \mu_l/(\rho_l D_A) \cong$

5000, for which by the use of the here applied resolution techniques a nearly mesh independent solution has been obtained. Considering, that for the forthcoming numerical example the corresponding Schmidt number is of an order of magnitude smaller offers the potential of obtaining even more accurate results.

Table 17.3: List of parameters used for the numerical simulations of the reacting small Taylor bubble problem. Diffusion coefficients have been determined by Krieger et al. [9].

Phase	ρ [kg/m^3]	μ [$10^{-3} \cdot$ Pa. s]	σ [N/m]	Species	D [$10^{-9} \cdot$ m^2/s]
Liquid	1000	1.12	0.075	A	2.0
Gas	1.2	0.018		B, C, D	0.6

17.4.2   Kinetic parameter estimation for reacting Taylor bubble flow

In this subchapter we will provide computational details for the application of reverse engineering technique in the framework of the reaction parameter estimation of a consecutive-competitive reaction system. The experimentally measured results – supporting the presented studies – were obtained by the chair of Laboratory of Equipment Design, Department of Biochemical and Chemical Engineering at the TU Dortmund. A detailed description of the corresponding innovative experimental setup is provided by Krieger et al. [8] which has utilized Arduino based regulation techniques for the camera movement during the experiments. The analyzed chemical reaction system corresponds to the oxidation of leuco-indigo carmine (B) to an intermediate (C) which then further oxidizes in the second step to keto-indigo carmine (D) according to the following reaction scheme:

$$A + B \overset{k_1}{\to} C \quad \text{and} \quad A + C \overset{k_2}{\to} D \tag{19}$$
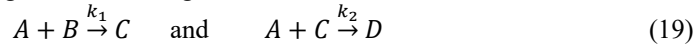
where the species (A) stand for oxygen. The chosen reaction system is not related to any industrially relevant production, however, due to the two distinct color changes of underlying oxidation steps it offers the advantage of spatial concentration measurements of the individual indigo species (B,C and D) at the same time. Additionally, due to the developed experimental technique of a sliding camera travelling with the liquid slug along the capillary the corresponding measurements could have been done not only spatially but also temporally in a highly resolved fashion. The reaction constants k_1 and k_2 – in the meantime also estimated by experimental techniques by Krieger et al. [9] – have been targeted to be determined by means of numerical simulations in a framework of reverse engineering techniques. As reference data the spatial distributions of the optically active species have been used at distinct time levels referring to 3.3 s, 6.6 s and at 11.0 s, with respect to the time elapsed from contacting the two phases, i.e. the bubble formation at the needle downstream in the capillary. The such generated bubbles were produced periodically leading to a periodic sequence of gas bubbles and liquid slugs. The liquid stream entering the capillary contained only species B of a concentration $c_{B:t=0} = 3 \cdot 10^{-4}$ mol/L , and no species of A,C and D, thus $c_{A,C,D:t=0} = 0 \cdot 10^{-4}$ mol/L. Oxygen has entered the system by blowing it periodically into the capillary through

the coaxial needle as a controlled volume air bubble, which due to the overall volumetric flow rate ($\dot{V}_t = \dot{V}_g + \dot{V}_l = 4.0$ cm³/min) were travelling through the capillary. The generated air bubbles began gradually releasing oxygen by means of mass transfer into the liquid slugs, which subsequently gave rise to the above described chemical reactions. The complete list of physical properties used for the numerical simulations is provided for the here considered system in Table 17.3.
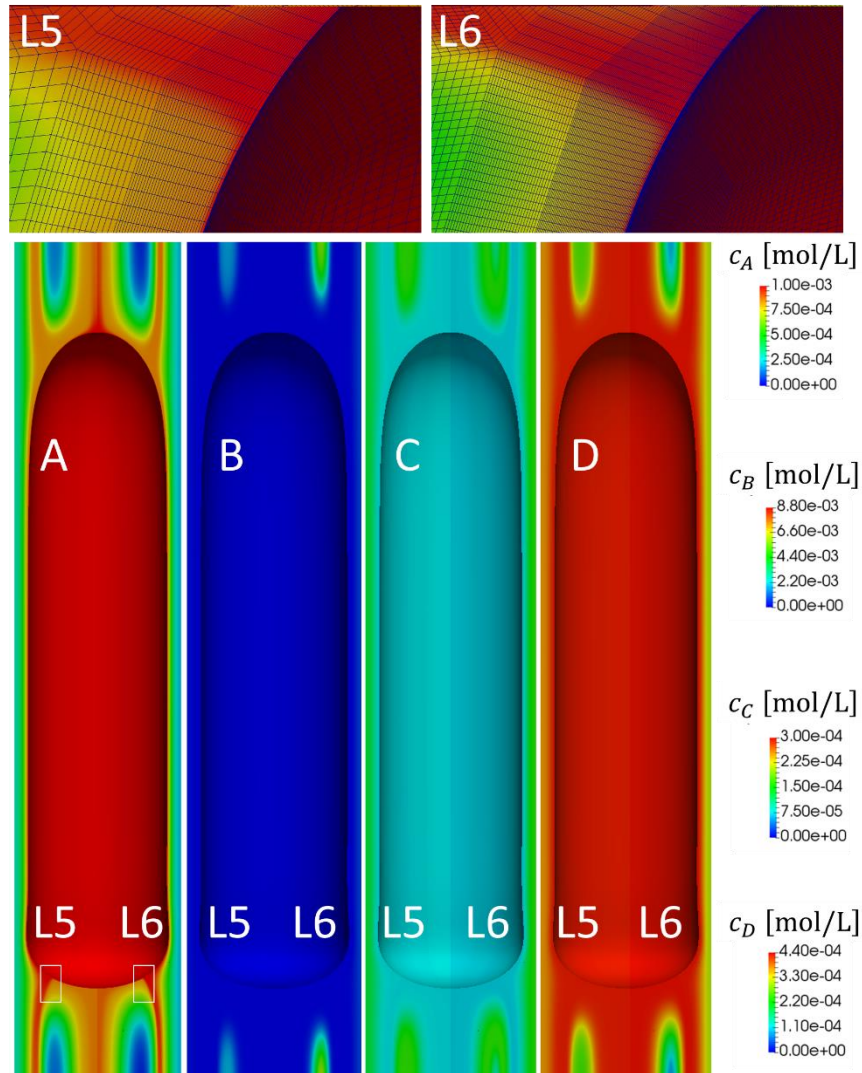
Figure 17.7: Mesh convergence of the scalar transport problem extended with chemical reactions after 2s of real time simulations. Top: two subpictures showing the distribution of the computationally most critical species A (oxygen) at the bubble surface and its wake on

mesh resolutions of Level 5 (left) and 6 (right). Bottom: concentration distribution of all A, B, C and D species with respect to the two considered mesh resolutions: L5 and L6.
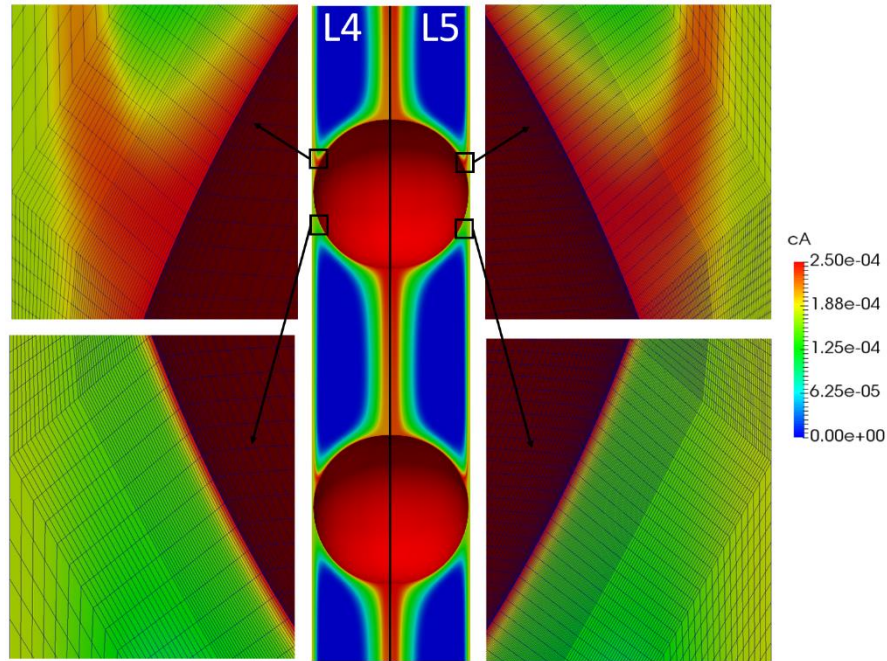
Figure 17.8: Visualization of the spatial convergence analysis of the reacting small Taylor bubble problem with mesh details. The full simulation domain with the corresponding concentration distribution is displayed in the middle for the two finest resolutions (L4 and L5) and at the sides close-ups of two representative regions at the bubble interface.

The numerical realization of the underlying problem has been done on the same basis as in the previously described example of Chapter 17.4.1 according to which only one single pair of a slug and bubble has been considered with the use of periodic boundary conditions at the inflow/outflow planes. Thus, the geometrical representation was restricted to a capillary of a diameter of $D = 1.6\ m$m and of length $L = 3.32\ m$m. The experimentally provided bubble volume – assuming to be constant due to neglecting its volume change due to mass transfer – has been $V_b = 1.98\ mm^3$ which has been initialized in the flow computations as a perfect sphere and in the course of the simulation sequences on low and high mesh resolutions it has reached its final steady shape. The underlying flow simulations were iterated with respect to the prescribed pressure drop as long as the requested flow rates have been achieved. The correspondingly obtained pressure drop was estimated as $\Delta p =$

3.3 Pa and the obtained flow field and interface distributions were used for the subsequent concentration transport equations with the corresponding chemical reactions.
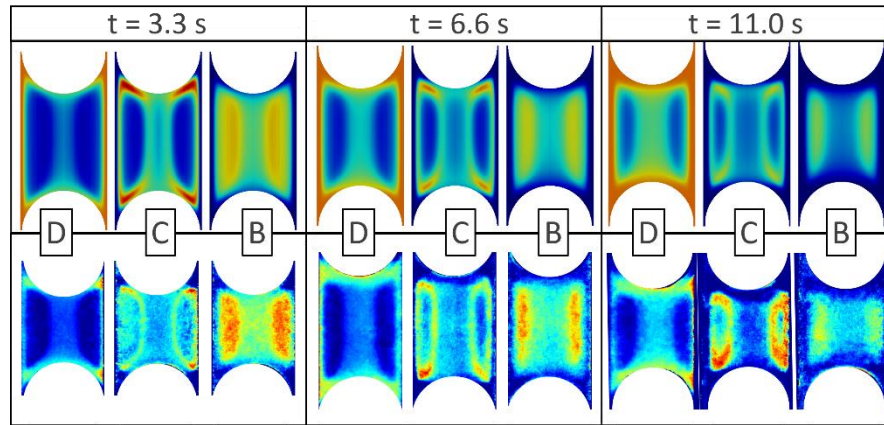
Figure 17.9: Comparison of the computationally obtained (top sequence) and experimentally measured (lower sequence) concentration distribution of the optically measurable species (B, C and D) at three reference time levels of $t = 3.3\ s, 6.6\ s$ and $11.0\ s$. The color scales refer to $0: 4 \cdot 10^{-4}\ mol/L$ for species B and D and $0: 4 \cdot 10^{-5}\ mol/L$ for species C.

As already described before, the gas bubble was represented in the numerical simulations of the concentration scalar equations only in terms of a Dirichlet boundary condition with respect to the oxygen species in the framework of a Henrys Law approximation. The corresponding value of this boundary concentration was represented by the value of $c_{A,\Gamma} = 2.5 \cdot 10^{-4}$ mol/L. The value of the characteristic Schmidt number for the here considered numerical simulations was $Sc = 330$, thus the use of the previously introduced meshing strategy in terms of the boundary layer resolution such as overall resolution was expected to provide nearly mesh independent solutions, as for the numerical example analyzed in Chapter 17.4.1. Accordingly, a graphical comparison of the two finest resolution level solutions for the found combination of kinetic parameters in terms of the oxygen concentration distribution is displayed in Figure 17.8 at the time level of $t = 6.6$ s. According to the inserted graphics, it can be seen that the concentration distribution of this most critical species A is nearly identical along the interfacial boundary surface and in the core of the liquid slug, as well. The values of the computationally found kinetic constants is $k_{1,comp} = 8.0 \cdot 10^5$ L/(mol. s) and $k_{2,comp} = 8.0 \cdot 10^5$ L/(mol. s) which compared to the experimentally found kinetic constants by Krieger et al. [9] $- k_{1,exp} = 6.3 \cdot 10^5$ L/(mol. s) and $k_{2,exp} = 22.4 \cdot 10^5$ L/(mol. s) – are matching reasonably well. According to the numerical simulations, the ratio of these two kinetic parameters is the most influential on the intermediate product C, which in case

that $k_1 : k_2 < 1.0$ clearly underpredicts the concentration of these intermediate species. Therefore, the experimentally determined combination of parameters was computationally not confirmed and the experimentally provided reference data could be reproduced in the most accurate way only with a ratio of $k_1 : k_2 = 1.0$.

It has to be noted that the comparison of the computational results with the experimental references had to be performed in a framework of a data transformation, which in particular means a projection of the full 3D data into a 2D representation, with the aim to provide a compatible analogy between the two (experimental and computational) methods. The corresponding representation of the results is presented in Figure 17.9, which shows the computational and the respective experimental concentration distributions at the three reference time levels. From the displayed sequence of pictures, it can be seen that the dynamics of the reaction is reasonably well captured – namely the consumption rate of B and the production rate of D – by the computations for the found kinetic parameters. Moreover, also the shape and the thickness of the characteristic ring of the intermediate product C is computationally resembled in a very good agreement with the experimentally recorded pictures.

17.5 Conclusion

In this study we have developed and demonstrated a reverse engineering framework applied in the field of single- and multiphase flows accompanied by chemical reactions. The computational strategy consisting of the individual numerical components has been applied for typical validation problems – mixing of species in a T-mixer [4] and the non-reacting Taylor bubble benchmark [11] – yielding fairly good agreement with the available reference results. Next, the basic flow modules (single- and multiphase) have been combined with the corresponding module of transport of species with chemical reaction and convergence estimation of the developed numerical simulation software has been performed. Based on the estimated necessary resolutions, the determination of reaction parameters has been performed for experimentally measured systems. The correspondingly estimated parameters have been proven to be in a very good accordance with assessments through independently performed experiments, which justifies that the use of the developed technique also in the framework of other possible reaction systems operating under the here considered assumptions. Moreover, the here developed numerical toolbox makes possible its application for detailed performance analysis of the chemical reactions in the framework of simple multiphase flows with respect to engineering quantities expressing the efficiency of the overall process like the yield of the wanted product or selectivity of a system of chemical reactions with respect to the desired product.

Acknowledgment

Reference

1. Adelsberger J., Esser P., Griebel M., Groß S., Klitz M., Rüttgers A.: 3D incompressible two-phase flow benchmark computations for rising droplets. Proceedings of the 11th World Congress on Computational Mechanics (WCCM XI), Barcelona, Spain, 2014.
2. Bayraktar E., Mierka O., Turek S.: Benchmark computations of 3D laminar flow around a cylinder with CFX, OpenFOAM and FeatFlow, International Journal of Computational Science and Engineering, 7(3), 253–266 (2012)
3. Boden S., Haghnegahdar M., Hampel U.: Measurement of Taylor bubble shape in square channel by microfocus X-ray computed tomography for investigation of mass transfer, Flow Measurement and Instrumentation 53, 49–55 (2017)
4. Bothe D., Lojewski A., Warnecke H.-J.: Computational analysis of an instantaneous chemical reaction in a T-microreactor, AIChE J., 56, 1406–1415 (2009)
5. Grajewski, M., Köster, M., Turek, S.: Mathematical and numerical analysis of a robust and efficient grid deformation method in the finite element context, SIAM J. Sci. Comput., 31(2), 1539–1557 (2008)
6. Hysing S.: Numerical Simulation of Immiscible Fluids with FEM Level Set Techniques. PhD Thesis, University of Dortmund, Dortmund, 2007
7. Hysing, S., Turek, S., Kuzmin, D., Parolini, N., Burman, E., Ganesan, S., Tobiska, L.: Quantitative benchmark computations of two-dimensional bubble dynamics. International Journal for Numerical Methods in Fluids, 60(11) (2009)
8. Krieger W., Hörbelt M., Schuster S., Hennekes J., Kockmann N.: Kinetic Study of Leuco-Indigo Carmine Oxidation and Investigation of Taylor and Dean Flow Superposition in a Coiled Flow Inverter. Chemical Engineering Technology, 42(10), 1–10 (2019)
9. Krieger, W., Bayraktar, E., Mierka, O., Kaiser, L., Dinter, R., Hennekes, J., Turek, S., Kockmann, N.: Arduino-based slider setup for gas-liquid mass transfer investigation: Experiments and CFD simulations, AIChE Journal, 66(6), (2020)
10. Kuzmin D., Turek S.: High-resolution FEM-TVD schemes based on a fully multidimensional flux limiter. Journal of Computational Physics, 198(1), 131–158 (2004)
11. Marschall H., Boden S., Lehrenfeld Ch., Falconi C. J., Hampel U., Reusken A., Wörner M., Bothe D.: Validation of Interface Capturing and Tracking techniques with different surface tension treatments against a Taylor bubble benchmark problem. Computers and Fluids 102, 336–352 (2014)

12. Mierka O., Munir M., Spille, C., Timmermann, J., Schlüter, M., Turek, S.: Reactive liquid flow simulation of micromixers based on grid deformation techniques, Chemical Engineering and Technology, 40(8), (2017)

13. Shampine L., Gordon M.: Computer Solution of Ordinary Differential Equations: The Initial Value Problem, Freeman, 1975, ISBN: 0716704617

14. Schumpe A., Lühring P.: Oxygen diffusivities in Organic Liquids at 293,2 K, J. Chem. Eng., 35, 24–25 (1990)

15. Schurr D., Strassl F., Liebhäuser P., Rinke G., Dittmeyer R., Herres-Pawlis S.: Decay kinetics of sensitive bioinorganic species in a SuperFocus mixer at ambient conditions, React. Chem. Eng., 5, (2016)

16. Toor H.L., Chiang S.H.: Diffusion-controlled chemical reactions, AIChE J., 5, 339–344 (1959)

17. Turek S.: On discrete projection methods for the incompressible Navier-Stokes equations: an algorithmical approach. Computer Methods in Applied Mechanics and Engineering, 143(3-4), 271–288 (1997)

18. Weiner A., Hillenbrand D., Marschall H., Bothe D.: Data-Driven Subgrid-Scale Modeling for Convection-Dominated Concentration Boundary Layers, Chemical Engineering & Technology, 42 (7), 1349–1356 (2019)

19. FeatFlow Homepage, www.featflow.de, version from July 2020